



Exploring the pore system of carbonate rocks through a multi-analytical approach

Silvia Salvini^{1,2} · Chiara Coletti¹ · Lara Maritan¹ · Matteo Massironi¹ · Fabrizio Balsamo³ · Claudio Mazzoli¹

Received: 23 August 2023 / Accepted: 11 October 2023 / Published online: 13 November 2023
© The Author(s) 2023

Abstract

The presence and distribution of pores in natural stones affect their durability and aesthetic value, especially when exposed to weathering agents like salt crystallization and freeze–thaw cycles. In this study, a multi-analytical approach was used to analyse the pore structure of twelve carbonate rocks, including different types of limestone and the Carrara marble. Mercury intrusion porosimetry, digital imaging analysis on backscattered electron images taken at the scanning electron microscope, and micro-computed tomography were used to overcome the limitations of each technique and create a more accurate reconstruction of the pore structure. This approach can aid in predicting the deterioration processes stones in heritage structures.

Keywords Porosity · Mercury intrusion porosimetry · Micro-computed tomography · Digital imaging analysis · Carbonate stones

Introduction

Despite the extensive literature on characterising the porosity of stones (Cnudde et al. 2009; Di Benedetto et al. 2015; Pappalardo et al. 2017; Scrivano et al. 2018; Benavente et al. 2021; Mineo and Pappalardo 2022), reliably estimating pore structure remains a challenge due to limitations of each analytical technique. Numerous methods have been developed to describe and quantify pore structure in rocks and porous materials, such as digital imaging analysis of scanning electron microscopy (SEM) images (Dal Sasso et al. 2014) and photomicrographs (Grove and Jerram 2011), mercury intrusion porosimetry (Leòn y Leòn 1998; Giesche 2006), water absorption (Molina et al. 2015), nitrogen adsorption (Rigby et al. 2004; Zong et al. 2015), X-ray micro-computed tomography (Cnudde et al. 2009; Fusi and Martinez-Martinez 2013; Noiriel 2015; De Kock et al. 2017), small angle

neutron scattering (Barbera et al. 2014), and nuclear magnetic resonance microscopy (Rijniers et al. 2005). However, discrepancies arise when comparing results from different techniques, which are often complementary as they analyse different pore size ranges (Anovitz and Cole 2015; Coletti et al. 2016). Combined approaches are necessary for a realistic reconstruction of the pore system in both natural and artificial stones (Barbera et al. 2014; De Boever et al. 2015; Coletti et al. 2016).

Detailed characterization of the pore structure is crucial in heritage conservation science as it affects the interaction of stone with environmental agents, such as rainwater, wind, and hygro-thermal changes, which ultimately impacts the deterioration rate of stone-made monuments and their vulnerability to loss of aesthetic value. This issue is particularly relevant for carbonate stones, which have been extensively used in historical built heritage and continue to be used as building materials due to their availability, load-bearing capacity, and workability (Fitzner and Basten 1994; Di Benedetto et al. 2015). However, they are more susceptible to water capillary absorption, dissolution, and erosion compared to silicate rocks. Salt crystallization cycles (Arnold and Zehnder 1990; Rodriguez-Navarro and Doehne 1999; Scherer 1999; Charola 2000; Doehne 2002; Sawdy and Price 2005; Steiger 2005; Cardell et al. 2008; Steiger and Charola 2011), wet-dry and freeze–thaw cycles (Nicholson 2001; Ruedrich and Siegesmund 2007; Grossi

✉ Chiara Coletti
chiara.coletti@unipd.it

¹ Department of Geosciences, University of Padova, Via Gradenigo 6, 25131 Padua, Italy

² Gallerie dell'Accademia di Venezia, Italian Ministry of Culture, Cannaregio 3553, 30121 Venice, Italy

³ Department of Chemistry, Life Sciences and Environmental Sustainability, University of Parma, Parco Area delle Scienze 157/A, Campus Universitario, 43124 Parma, Italy

et al. 2007; Ruedrich et al. 2011), the formation of gypsum crusts (Bugini et al. 2000) and biological colonization (Warscheid and Braams 2000; Gabriele et al. 2023) are among the most effective mechanisms of carbonate rock deterioration. Furthermore, porosity also influences the physical and mechanical properties of the stones utilised as building materials. Hydric properties, such as water adsorption, drying index, and capillary coefficient, dynamic properties such as propagation velocity of compressional and shear ultrasound pulses, Young's modulus, shear modulus, bulk modulus, Poisson's ratio, compressive strength, flexural strength, and point load strength, are all heavily reliant on the types of pores, their interconnection, dimensions, pore-size distribution, and the complexity and heterogeneity of microstructures (Benavente et al. 2004; García-del-Cura et al. 2012; Molina et al. 2015; Koubaa et al. 2018; Yang et al. 2023). Triaxial deformation experiments conducted across the brittle-ductile transition have demonstrated the significance of initial porosity on deformational behaviour in limestone under different deformation rates, as well as the evolution of the pore system during loading (Brantut et al. 2018). Ng and Santamarina (2023) have shown that mechanical and hydraulic properties are strongly dependent on porosity, and have discovered that a power model provides a good approximation for global trends of unconfined stiffness, unconfined compressive strength, cohesive intercept in Mohr–Coulomb failure envelopes, and brittle-to-ductile transition stress versus porosity. Consequently, changes in porosity due to stone deterioration, or the dissolution of rock formations due to water circulation as seen in karstic environments, can have complex effects on their mechanical properties and can lead to failure under external stresses, or alter the geomechanical properties of rock masses (Niazi et al. 2021). Despite being generally viewed as a weakness factor, porosity, especially when abundant or when pores are large in size, can confer some advantageous properties in terms of thermal and acoustic insulation, offering clear benefits in energy efficiency (Di Benedetto et al. 2015). In this work, we determined the pore structure of twelve carbonate rocks, including eleven types of limestone quarried from northeastern Italy and Croatia, and the Carrara marble, derived from the Apuan Alps (northern Tuscany region, central Italy), which have been widely used in the Italian built heritage. This study aims to increase our understanding of pore characterization in carbonate stones, particularly those used in cultural heritage. For this reason, several methods were employed to reveal the widest possible pore-size range. Porosity and pore space distribution in limestones result from many processes, both depositional and post-depositional, and thus, they exhibit significant variations (Benavente et al. 2004; Benavente 2011). The Carrara marble, a prestigious and popular stone used in sculpture and building décor since Roman times, is a carbonate

metamorphic rock that can undergo to the same deterioration mechanisms as limestones (Salvini et al. 2022, 2023).

The porosity of the stones was studied using a multi-analytical approach, consisting in the analysis by mercury intrusion porosimetry (MIP), digital imaging analysis (DIA) of backscattered electron (BSE) images obtained by scanning electron microscopy (SEM), and 3D reconstructions obtained by micro-computed tomography (m-CT), following the procedure proposed in Coletti et al. (2016). Since various pore-size classifications are reported in the literature (De Quervain 1967; Choquette and Pray 1970; Dubinin 1979; Gregg and Sing 1983; Klopfer 1985; Kodikara et al. 1999), in this work it was adopted that proposed by De Quervain (1967) and discussed in Siegesmund and Dürrast (2011); pores were classified as micropores (radius $< 5 \mu\text{m}$), mesopores (radius $5\text{--}200 \mu\text{m}$), and macropores (radius $200\text{--}2000 \mu\text{m}$).

Materials and methods

Materials

This study focuses on twelve different types of carbonate rocks that are commonly used as building and ornamental materials in historical monuments and constructions in Italy. These rock types are from different geological formations outcropping in northeastern Italy, Croatia, and in the Apuan Alps (northern Tuscany, central Italy). For a detailed description of their geological and petrographical features, refer to Salvini et al. (2023). Table 1 lists the name, label, provenance, and general geological information of each rock type. The study includes the Pink and White Asiago stones (RO and BI, respectively), the Red and Brown Verona stones (RV and BV, respectively), the Vicenza stones (Nanto variety, NA; and Costozza variety, CO), the Chiampo stones (two varieties: Paglierino, PA; and Ondagata, ON), the Boticino stone (BO), the Aurisina stone (AU), the Istria stone (Orsera variety, OR), and the Carrara marble (M).

Methods

Porosity was examined combining mercury intrusion porosimetry (MIP), digital image analysis (DIA) of backscattered (BSE) images acquired by scanning electron microscopy (SEM) and X-ray micro-computed tomography (micro-CT). Pore system was described accounting for the pore-size distribution obtained with the different methods by defining “overlapping pore ranges” and considering the limitations of each technique within specific pore-size intervals. A description of the analytical conditions and the data processing follows.

Table 1 Simplified summary description of rock types considered in this work

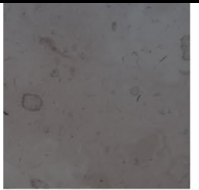
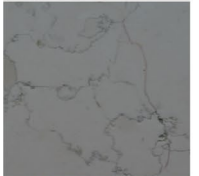
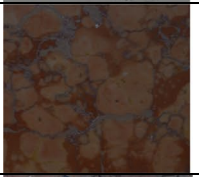


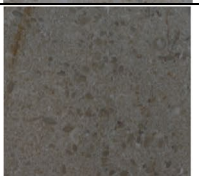
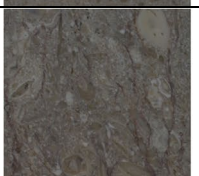
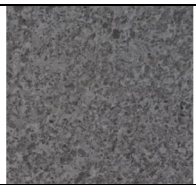


Area	Common name	Variety	Label	Rock type	Geological Formation	Macroscopic appearance
Northeastern Italy	Asiago stone	Pink Asiago	RO	Mudstone/Wackestone	Maiolica F.	
		White Asiago	BI			
	Verona stone	Red Verona	RV	Wackestone	Rosso Ammonitico Veronese F.	
		Brown Verona	BV			
	Vincenza stone	Nanto	NA	Packstone/Rudstone	Nummulitic Limestone F.	
		Costozza	CO	Grainstone/Rudstone		Castelgomberto Limestone F.
Chiampo stone	Paglierino	PA	Rudstone	Nummulitic Limestone F.		
	Ondagata	ON				
	Botticino stone	BO			Floatstone/Crystalline carbonate	Corna F.

Table 1 (continued)

	Aurisina stone		AU	Rudstone/Grainstone	Sežana and Lipica F.	
Croatia	Istria stone	Orsera	OR	Mudstone	Kirmenjakk Unit	
Central Italy	Carrara marble		M	Marble	Tuscan Nappe	

In the photographs, the sample dimensions have sides measuring 2 cm

MIP was performed using a PoreMaster 33 system (Quantachrome Instruments[®]), which has a sample cell of 1.0×3.0 cm and a volume of 2 cm^3 . The pressure range is 0.5–33,000 psi; considering a contact angle (θ) of mercury of 140° , and a surface tension (σ) of mercury of 0.48 N/m (480 dyn/cm), the investigated pore size range is from 0.0064 to 950 μm . Before the measurements, samples were dried at 40°C for 24 h and then about 2 g (i.e. a core 2 cm long with a diameter of 8 mm) of material was analysed.

Scanning electron microscopy back-scattered electron (SEM-BSE) images were obtained by scanning the thin sections according to a matrix of 30×40 SEM-BSE images that were overlapped by 25%. For each sample, a total of 1200 images were acquired with a resolution of 1280×1024 pixels at a magnification of $200 \times$, using a CamScan MX 2500 microscope equipped with a LaB_6 cathode. The microscope operated at 20 kV with a working distance (WD) of 20 mm.

The grey-scale images were segmented, binarized, and analysed using the ImageJ[®] software, which is a public Java domain image processing tool. The Digital Images Analysis (DIA) of pore size was based on the measure of the Feret diameter. The Feret diameter is defined as the distance between the two parallel planes that restrict the object perpendicular to that direction in 2D (Rasband 1997–2015; Maritan et al. 2020). The limit of resolution was determined to be 0.5 μm , which corresponds to one pixel.

For each stone type, micro-cores with a diameter of 8 mm and a length of 20 mm were analysed using a bench-top Skyscan 1172 micro-CT scanner by Bruker[®]. The micro-CT scanner was equipped with a Hamamatsu 100/250 micro-focus X-ray source, operating at an acceleration voltage of 74 kV and a beam current of 133 μA . The system used a

Hamamatsu C9300 10-megapixel camera with a pixel size 8.5 μm , and the X-ray beam was filtered by a 0.5 mm Al foil. Projection images were acquired at 0.3° intervals over a 360° rotation, with an exposure time of 2500 ms and a camera binning of 2×2 . To minimise noise, 8 frames were averaged in vertical random movement mode, and 3 scans were connected to cover the entire vertical length of the cores. Each scan took approximately 21 h to complete. Cross-section slices were reconstructed from raw projection images using the NRecon software by Bruker[®], which included application of thermal correction, misalignment compensation, ring artefact reduction and beam hardening correction. Porosity was segmented by thresholding tomographic images with the CT-Analyser software by Bruker[®], resulting in binary image stacks. Porosity was calculated as the ratio of the number of voxels of the pores (pore-voxels) to the total Volume Of Interest (VOI) (Coletti et al. 2016). Structural thickness was used to measure pore size diameters and distribution. It involved fitting maximal spheres inside the structure and determining the value of the largest sphere contained within it. The limit of resolution for this analysis was set to 4.75 μm , which corresponds to a minimum volume unit (voxel) of approximately $107 \mu\text{m}^3$.

Results and discussion

Mercury intrusion porosimetry

Based on the MIP results, the twelve studied rocks can be categorised into three different groups based on their total percentage of pores (refer to Table 2, Fig. 1). The first group

Table 2 Results from mercury intrusion porosimetry

	RO	BI	RV	BV	NA	CO	PA	ON	BO	AU	OR	M
Total porosity	3.55	2.20	0.32	0.10	27.17	28.52	0.57	1.10	1.72	4.61	0.40	1.06
Ø max	216	215	379	394	371	221	221	216	235	273	211	215
Pore size range												
<0.5	2.27	1.80	0.06	–	11.90	11.24	0.21	0.02	1.24	3.69	–	0.36
0.5–2.5	–	–	0.06	–	15.11	2.10	0.21	0.02	0.05	0.01	–	–
2.5–4.75	–	–	0.01	–	–	0.20	0.01	–	–	–	–	0.06
4.75–24	–	–	0.07	–	0.02	6.06	0.02	0.06	–	0.21	0.06	0.08
24–50	–	–	–	–	0.02	6.43	–	0.16	–	0.19	0.04	0.04
50–70	0.02	0.12	–	–	–	0.89	–	0.03	–	0.12	0.01	0.08
70–100	0.11	0.04	–	0.05	–	0.73	0.02	0.18	0.01	0.12	0.07	0.07
100–150	0.48	0.10	0.03	0.01	0.00	0.62	–	0.20	0.22	0.10	0.06	0.21
150–200	0.57	0.11	0.02	0.01	0.03	0.25	0.02	0.37	0.17	–	0.13	0.14
200–250	0.10	0.03	–	0.01	–	–	–	0.06	0.03	0.13	0.03	0.02
>250	–	–	0.07	0.02	0.09	–	0.08	–	–	0.04	–	–

Total porosity (%); Ø max = maximum diameter or pores (µm); porosity (%) according to the different pore size ranges (µm)

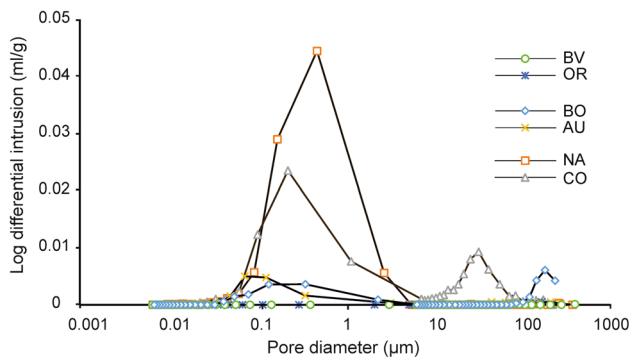


Fig. 1 Pore-size distribution of stones representative for the three groups of samples based on their total percentage of pores: group 1 (total porosity below 1%): Orsera stone (OR) and Brown Verona stone (BV); group 2 (total porosity ranging from 1 and 5%): Aurisina stone (AU) and Botticino stone (BO); group 3 (total porosity exceeding 20%): Nanto stone (NA) and Costozza stone (CO)

(group 1) consists of samples with total porosity below 1.00%. This group includes four samples: both the varieties of Verona stone (Red Verona stone, RV, and Brown Verona stone, BV) with porosities of 0.32% and 0.10%, respectively), the Paglierino stone (PA), a variety of the Chiampo stone, which displays a porosity of 0.57%, and the Orsera stone (OR), with a porosity of 0.40%. The second group (group 2) consists of samples with total porosity ranging from 1 and 5%. Most of the stones fall into this group. The Aurisina stone (AU) exhibits the highest total percentage of porosity at 4.61%, followed by the two varieties of Asiago stone, the Pink Asiago stone, (RO), with 3.55%, and the White Asiago stone (BI) with 2.20%, the Botticino stone (BO) with 1.72%, and the Carrara marble with 1.00%. In these two groups (groups 1 and 2) the majority of pores are

micropores (Fig. 1), mostly below 0.5 µm (Table 2). The third group (group 3) includes samples with high porosity, exceeding 20%, represented by the two varieties of Vicenza stones (Fig. 3). The Nanto stone (NA) displays 27.17% of pores, with over 90% of them being definable as micropores (De Quervain 1967; Siegesmund and Dürrast 2011): 11.90% in the range <0.5 µm, and 15.11% in the range comprised between 0.5 and 2.5 µm (Table 1). The Costozza stone (CO) exhibits 28.52% of pores. The pores are distributed with a bimodal distribution (Fig. 1): 13.34% of pores fall within the range of pores with a diameter below 5 µm, but almost half of them can be classified as mesopores (De Quervain 1967; Siegesmund and Dürrast 2011) in the ranges of 4.75–24 µm (6.06% of pores) and 24–50 µm (6.43%) (Table 2).

Despite the wide range of the total porosity, all samples exhibited a maximum pore size exceeding 200 µm (Ø max in Table 2). The significant percentage of pores below 0.5 µm observed in some of the samples may be attributed to a potential overestimation of the smallest pores, known as the “ink bottle effect”. This effect is a well-known limitation of the MIP analytical technique (Moro and Böhni 2002; Dal Ferro et al. 2012).

Porosity by digital imaging analysis of SEM-BSE images

Digital imaging analysis (DIA) was conducted on stitched SEM-BSE images, combining 1200 images per sample, to obtain a representative area on which to perform the analysis of pore-size distribution (Fig. 2). The DIA data aligned well with the results from MIP analysis for samples belonging to group 3 (porosity exceeding 20%), which included the two varieties of Vicenza stone: the Nanto stone (NA) with

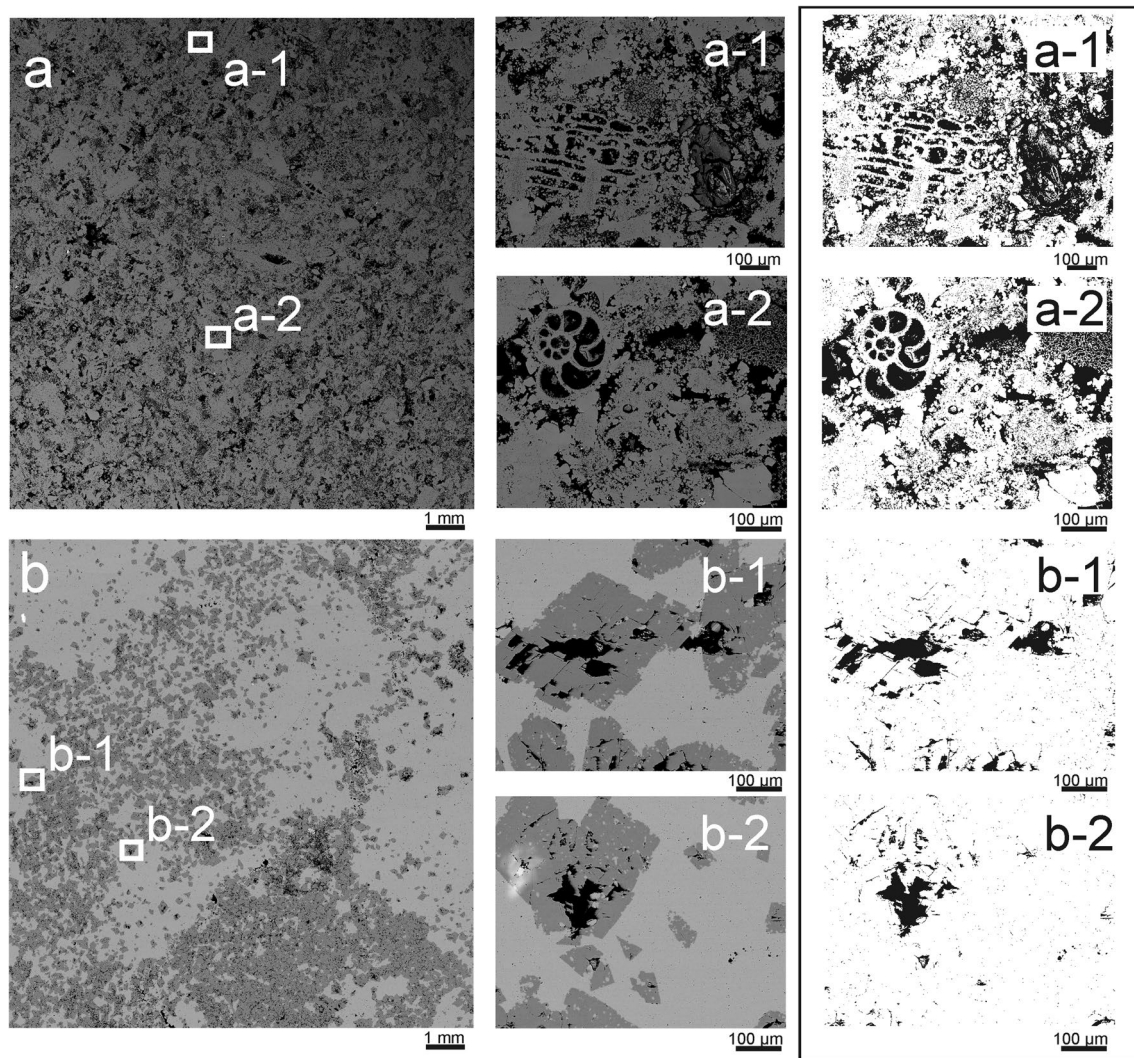


Fig. 2 SEM-BSE images of Nanto stone (NA) and Botticino stone (BO). **a** Panoramic image of NA obtained by stitching SEM-BSE images acquired at a magnification of 200; **a-1** and **a-2** Two of the 1200 SEM-BSE images used in the photo stitching process. **b** SEM-BSE panoramic image of BO obtained using the same method as

described for NA; **b-1** and **b-2** Two of the 1200 SEM-BSE images used in the photo stitching process. The images in the right-hand box are the binarized one, with pores shown in black, obtained by the pores segmentation

24.97% of total porosity (Fig. 2a, a-1, a-2) and the Costozza stone (CO) with 17.33%. Differences arises when the total porosity values for samples in groups 1 and 2 (total porosity below 1% and ranging from 1 and 5%, respectively) as obtained by DIA are compared to those got by MIP. Most of the samples exhibited a total porosity below 1%, influencing their classification into groups 1 and 2 based on MIP data. Verona stones (BV and RV) and Asiago stones (RO and BI) had very low porosity, generally below 0.25%. In contrast, Botticino stone (BO) (Fig. 2b, b-1, b-2) and Carrara marble (M) displayed porosities of 4.11% and 2.11%, respectively. These discrepancies between DIA and MIP results can be explained by the fact that DIA has a fixed threshold limit of 0.5 μm , disregarding any information about pores below

this diameter, which is particularly relevant for these types of samples (as indicated by MIP, Table 2). On the other hand, DIA provides reliable information about macropores (De Quervain 1967; Siegesmund and Dürrast 2011). This is clearly evident in the estimation of pore sizes in the largest range size (250–360 μm) reported in Table 3, as well as in Fig. 2.

NA and CO exhibited the highest percentages of pores in the larger pore size ranges (200–250 μm and 250–360 μm). In fact, over 50% of the total porosity of NA and over 30% of CO were referable to pores larger than 250 μm . Pores generally had maximum diameters ranging from 100 and 300 μm . As expected, the largest pores were found in the Vicenza stones, with the Costozza stone (CO) and Nanto

Table 3 Results from DIA of SEM-BSE images acquired at a magnification of 200

	RO	BI	RV	BV	NA	CO	PA	ON	BO	AU	OR	M
Total porosity	0.17	0.24	0.64	0.03	24.97	17.33	0.95	1.63	4.11	0.61	0.43	2.11
Ø max Feret	66	319	181	134	2067	584	285	112	320	235	169	233
Pore size range												
0.5–2.5	–	0.05	0.22	–	0.49	1.11	0.17	0.90	0.13	0.16	0.03	0.06
2.5–4.75	0.02	0.05	0.11	0.01	0.74	1.00	0.19	0.37	0.24	0.11	0.05	1.09
4.75–25	0.10	0.09	0.18	0.01	3.25	2.10	0.37	0.30	1.84	0.21	0.17	0.49
25–50	0.01	0.02	0.04	–	2.17	1.33	0.09	0.02	0.90	0.05	0.07	0.11
50–70	0.04	0.01	0.01	0.01	1.37	0.97	0.04	–	0.35	0.02	0.03	0.08
70–100	–	–	0.03	–	1.55	1.46	0.02	0.01	0.26	0.02	0.04	0.09
100–150	–	0.01	0.02	–	2.13	2.16	0.03	0.00	0.25	0.01	0.03	0.13
150–200	–	–	0.03	–	1.69	1.98	0.02	0.03	0.10	–	0.01	0.02
200–250	–	–	–	–	1.47	1.78	0.01	–	0.04	0.03	–	0.04
250–360	–	0.01	–	–	10.11	3.44	0.02	–	0.22	–	–	–
>360	–	–	–	–	7.85	2.06	–	–	–	–	–	–

Total porosity (%); Ø max Feret=maximum Feret diameter (µm); porosity (%) according to different pore size ranges (µm)

stone (NA) displaying the maximum pore diameters of 584 and 2067 µm, respectively. Both of these rocks showed a considerable fraction of porosity above 360 µm (Table 2), accounting for 8% in the case of Nanto stone, and 2% in the Costozza stone.

Porosity by micro-CT measurements

The total porosity measured by m-CT shows values ranging between 0.25 and 1.50% (Table 4). However, Vicenza stones, NA and CO, exhibit higher porosity, 8.96% and 13.53% respectively, in agreement with measurements obtained by MIP and DIA.

Botticino stone (BO) and Carrara marble (M) have total porosity of 1.30% and 0.04% respectively (Table 3). These

values are lower when compared to DIA, possibly due to the different threshold size limits adopted in the two analytical methods: 0.5 µm for DIA and 4.75 µm for m-CT. Most of the pores have diameters below 20 µm (Table 4), which is consistent with observations made by MIP and DIA.

Figure 4 presents the reconstructed images of four samples obtained from m-CT acquisitions, along with their relative segmented and binarized images. The 3D stacks of binarized slices not only visually confirm the data reported in Table 3 but also provide additional valuable information. For instance, in the Brown Verona stone (BV, Fig. 3a), although its porosity is low (Table 4), the 3D distribution of its voids reveals the presence of microstructural discontinuities within the specimen (Fig. 3a). On the other hand, in the Costozza stone (CO, Fig. 3b), porosity is high and

Table 4 Results from the m-CT analysis

	RO	BI	RV	BV	NA	CO	PA	ON	BO	AU	OR	M
Total porosity	0.28	1.04	0.27	0.07	8.96	13.53	0.73	1.50	1.30	1.21	1.07	0.04
Ø max	23	33	42	71	308	241	33	33	147	270	90	33
FD	2.69	2.83	2.69	2.36	2.72	2.85	2.80	2.86	2.63	2.46	2.80	2.28
Pore-size range												
4.75–25	0.28	1.04	0.27	0.07	6.57	6.43	0.73	1.50	1.22	0.44	1.05	0.04
25–50	–	–	–	–	1.73	4.32	–	–	0.08	0.44	0.02	–
50–70	–	–	–	–	0.51	1.26	–	–	0.00	0.13	–	–
70–100	–	–	–	–	0.08	0.93	–	–	–	0.10	–	–
100–150	–	–	–	–	0.05	0.46	–	–	–	0.06	–	–
150–200	–	–	–	–	0.02	0.11	–	–	–	0.02	–	–
200–250	–	–	–	–	–	0.02	–	–	–	0.01	–	–
>250	–	–	–	–	–	–	–	–	–	0.01	–	–

Total porosity (%); Ø max=maximum structural thickness (µm); FD=fractal dimension; porosity (%) according to different pore-size ranges (µm)

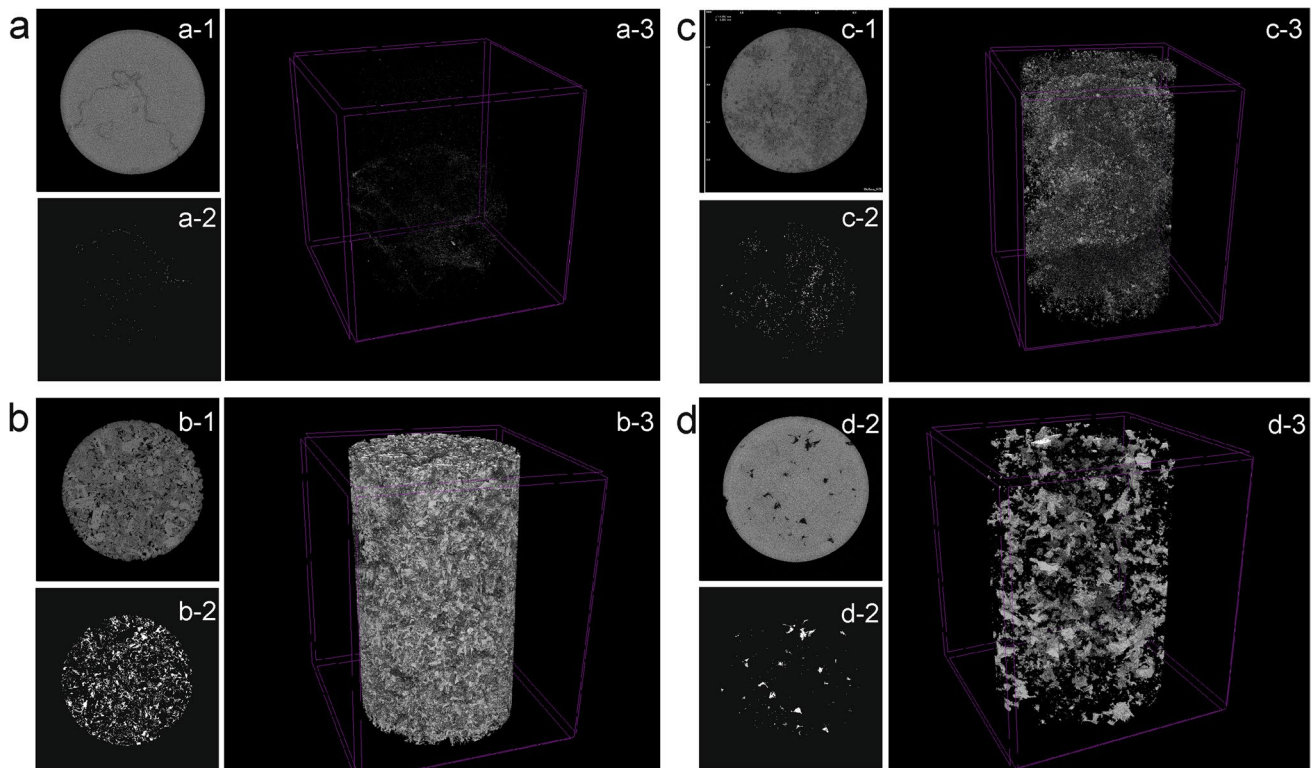


Fig. 3 Some results obtained by m-CT: **a** Brown Verona stone (BV); **b** Costozza stone (CO); **c** Botticino stone (BO); **d** Aurisina stone (AU). **a-1, b-1, c-1** and **d-1** Single reconstructed images; **a-2, b-2, c-2**

and **d-2** Corresponding segmented and binarized images; **a-3, b-3, c-3** and **d-3** 3D reconstructions obtained from stacks of segmented and binarized images. Core diameter: 7.6 mm

uniformly distributed within the core (Fig. 3c). The Botticino stone (BO) and the Aurisina stone (AU), which display similar total porosities (1.30% and 1.21% respectively; see Table 4), exhibit contrasting pore structures in terms of size and distribution (Fig. 3c, d). Stone BO is characterized by a dense network of small-diameter pores (Fig. 3c), while AU displays larger pores connected each other by channels of varying diameter (interconnected pores).

The Fractal Dimension (FD) used as an indicator of the pore surface complexity, was calculated using the Skyscan CT-analyser software employing the ‘box-counting’ method. This method involves dividing the object into a grid of boxes of varying sizes and counting the number of boxes that contain some part of the object. As the size of the boxes decreases, the number of boxes needed to cover the object increases. By plotting the relationship between the box size and the number of boxes required on a log–log graph, valuable information about the scaling behaviour of the object is obtained, allowing for the estimation of its Fractal Dimension. The Fractal Dimension is then determined from the slope of the log–log regression (Chappard et al. 2001). In the studied materials, FD ranges between 2 and 3 in Euclidean space. Smooth surfaces typically have a value of 2. The calculated values for the analysed samples fall in the range

of 2.36 and 2.86, confirming the true fractal behaviour of the pore system, which exhibits self-similarities at various scales (Table 4).

Comparing results from the different techniques

Most of the studied rocks exhibited low total porosity below 5% (Tables 2, 3 and 4). However, the two types of Vicenza stones (NA and CO) showed significantly higher values above 10% or 20%, depending on the specific analytical method employed (Tables 2, 3 and 4).

Total porosity measured by MIP (Table 2) was generally higher than that obtained by DIA and m-CT (Tables 3 and 4). These differences may be explained by the fact that the latter analytical techniques have a threshold limit, represented by the minimum detectable pore dimension. In our case, this limit was 0.5 μm for DIA on SEM-BSE images and 4.75 μm for m-CT. The specific setup used during the acquisition sessions determines these threshold values. As a result, DIA and m-CT tended to underestimate the total porosity. This issue is particularly evident in samples where a significant fraction of the porosity falls below the analytical thresholds mentioned above. For instance, in rocks such as RO, AU, and BI, where the highest percentage of pores

is within the pore range below 0.5 μm, DIA on SEM-BSE images underestimated the porosity. To address this limitation, it is essential to consider the fraction of pores below 0.5 μm, as estimated by MIP.

A similar consideration can be made when interpreting results from m-CT analysis. This method tended to underestimate the total porosity, especially in samples with prevailing micropores, as pores with diameter below 4.75 μm were not measured. The discrepancy in porosity obtained by m-CT with respect to measurements obtained by MIP and DIA (Tables 2 and 3) is also evident in samples with a larger pore range, such as stones NA and CO (Table 4). Thus, in order to better compare the results obtained by MIP, DIA and m-CT, the porosity fraction pertaining to specific pore ranges was considered for the different methods.

Table 5 presents the percentage of porosity categorized into specific pore ranges, extrapolated from Tables 2, 3 and 4. These ranges include: (i) pores below 0.5 μm, determined using MIP; (ii) pores between 0.5 and 4.75 μm, with partial results obtained though MIP and DIA (the lower limit of 0.5 μm, corresponds to the threshold for DIA imposed by the analytical procedure adopted, while the upper limit of 4.75 μm corresponds to the lower threshold of m-CT); (iii) pores between 4.75 and 360 μm, with partial results obtained through MIP, m-CT and DIA; (iv) pores above 360 μm, detected exclusively by DIA.

The “overlapping pore ranges” (0.5–4.75 μm and 4.75–360 μm) reveal slight or significant differences in the estimation of pores abundance across the various methods.

Notably, porosity within the first “overlapping pore range” (OPR-1: 0.5–4.75 μm, as shown in Table 5) demonstrated the superior accuracy of DIA. In fact, while MIP measurements yielded no discernible porosity within this range in two-third of the samples, DIA analysis unveiled a substantial presence of pores.

The lower porosity values in this range measured by MIP may be attributed to the “ink-bottle effect” which tends to underestimate the real pore size in this range, as well as to the irregular shapes of voids that can collapse at high pressure during mercury intrusion, especially in highly porous and weaker materials (Moro and Böhni 2002; Giesche 2006;

Galaup et al. 2012). This behaviour may explain the higher porosity detected by MIP in such samples (e.g. sample NA displays 15.11% of pores detected by MIP compared to 1.33% of pores observed with DIA).

Results in the second “overlapping pore range” (OPR-2: 4.75–360 μm, Table 5) are quite similar for all the methods used, except for stone NA, which shows 0.17% of pores obtained using MIP, 15.90% of pores according to DIA, and 8.96% of pores estimated by m-CT. The underestimation of MIP data in this interval is compensated by an overestimation in the lower overlapping pore range OPR-1, and, as discussed above, it can be related to the “ink bottle effect”. The difference between DIA and m-CT may also be due to sample damage during the thin section preparation. The presence of fractures and circum-granular detachments will result in a partial overestimation of porosity. The representativeness of the sample can also be an issue in samples of strongly heterogeneous materials.

Moreover, the values of total porosity measured by DIA and m-CT are often higher than those measured by MIP (e.g. Botticino stone, BO, 3.79% and 1.30% estimated by DIA and m-CT, respectively, compared to 0.43% measured by MIP, OPR-2, Table 5). This can be attributed to the presence of closed pores not measured by MIP, but accessible by DIA and m-CT.

Pore estimation and cumulative curves

Based on the differences in the pore size distribution obtained from the different analytical methods and comparing the results within specific “overlapping pore ranges” (OPR-1 and OPR-2, see Table 5), we were able to establish specific pore size intervals where each method provided reliable data. We used this information to estimate the total porosity (Table 6), and create a reliable cumulative pore size distribution curve (Fig. 4) by appropriately combining data from MIP, DIA, and m-CT pore distributions (Tables 2, 3 and 4).

Specifically, the total porosity and the pore size distribution curve were determined using the following combinations: (i) results obtained from MIP (indicated as “MIP”

Table 5 Summary of porosity referred to specific pore size ranges and “overlapping pore ranges” (OPR-1 and OPR-2) obtained using different analytical techniques (MIP, DIA and m-CT)

Pore size range	Method	RO	BI	RV	BV	NA	CO	PA	ON	BO	AU	OR	M
<0.5	MIP	2.27	1.80	0.06	–	11.90	13.34	0.21	0.02	1.24	3.70	–	0.30
OPR-1 0.5–4.75	MIP	–	–	0.01	–	15.11	–	0.01	–	0.06	–	–	0.04
	DIA	0.02	0.10	0.33	0.01	1.33	2.11	0.36	1.36	0.45	0.30	0.08	1.15
OPR-2 4.75–360	MIP	1.27	0.39	0.19	0.10	0.17	15.18	0.14	1.02	0.43	0.92	0.39	0.66
	DIA	0.15	0.14	0.31	0.02	15.90	13.12	0.59	0.36	3.79	0.32	0.34	0.96
	m-CT	0.28	1.04	0.27	0.07	8.96	13.51	0.73	1.50	1.30	1.20	1.07	0.04
> 360	DIA	–	–	–	–	7.85	2.06	–	–	–	–	–	

Values are expressed as a percentage (%)

Table 6 Total porosity (%) estimated by appropriately combining the results from different methods (MIP, DIA and m-CT) within specific pore size intervals

Method	RO	BI	RV	BV	NA	CO	PA	ON	BO	AU	OR	M
MIP	3.54	2.20	0.32	0.10	27.17	28.52	0.57	1.10	1.72	4.61	0.40	1.06
MIP + DIA	2.44	2.04	0.70	0.03	36.98	30.33	1.59	1.71	5.64	4.22	0.42	2.43
MIP + m-CT	2.55	2.84	0.34	0.07	35.99	27.15	1.37	1.51	2.60	4.95	1.07	0.40
St.D. _(MIP+DIA vs MIP)	0.78	0.11	0.27	0.05	6.94	1.28	0.72	0.43	2.77	0.28	0.01	0.97
St.D. _(MIP+m-CT vs MIP)	0.71	0.45	0.01	0.02	6.24	0.97	0.57	0.29	0.62	0.24	0.47	0.47

St.D._(MIP+DIA vs MIP) and St.D._(MIP+m-CT), represent the standard deviations calculated between the total porosity values (%) measured by MIP and those obtained through the combined approaches with DIA (St.D._(MIP+DIA vs MIP)) and m-CT results (St.D._(MIP+m-CT))

in Table 6 and represented by the blue line in Fig. 4); (ii) porosity and pore size distribution curve defined by the MIP results up to 2.5 μm , followed by the pattern obtained using DIA (indicated as “MIP + DIA” in Table 6 and represented by the red dotted line in Fig. 4); (iii) porosity and pore size distribution curve defined by the MIP results up to 4.75 μm , followed by the pattern obtained using m-CT (indicated

as “MIP + m-CT” in Table 6 and represented by the green dashed line in Fig. 4).

For the Nanto stone (sample NA), as the results are strongly affected by the “ink-bottle effect”, we set the MIP limit for the DIA curve (“MIP + DIA” in Table 6 and Fig. 4) to 0.5 μm (Table 2), which ensured a good agreement between the various techniques.

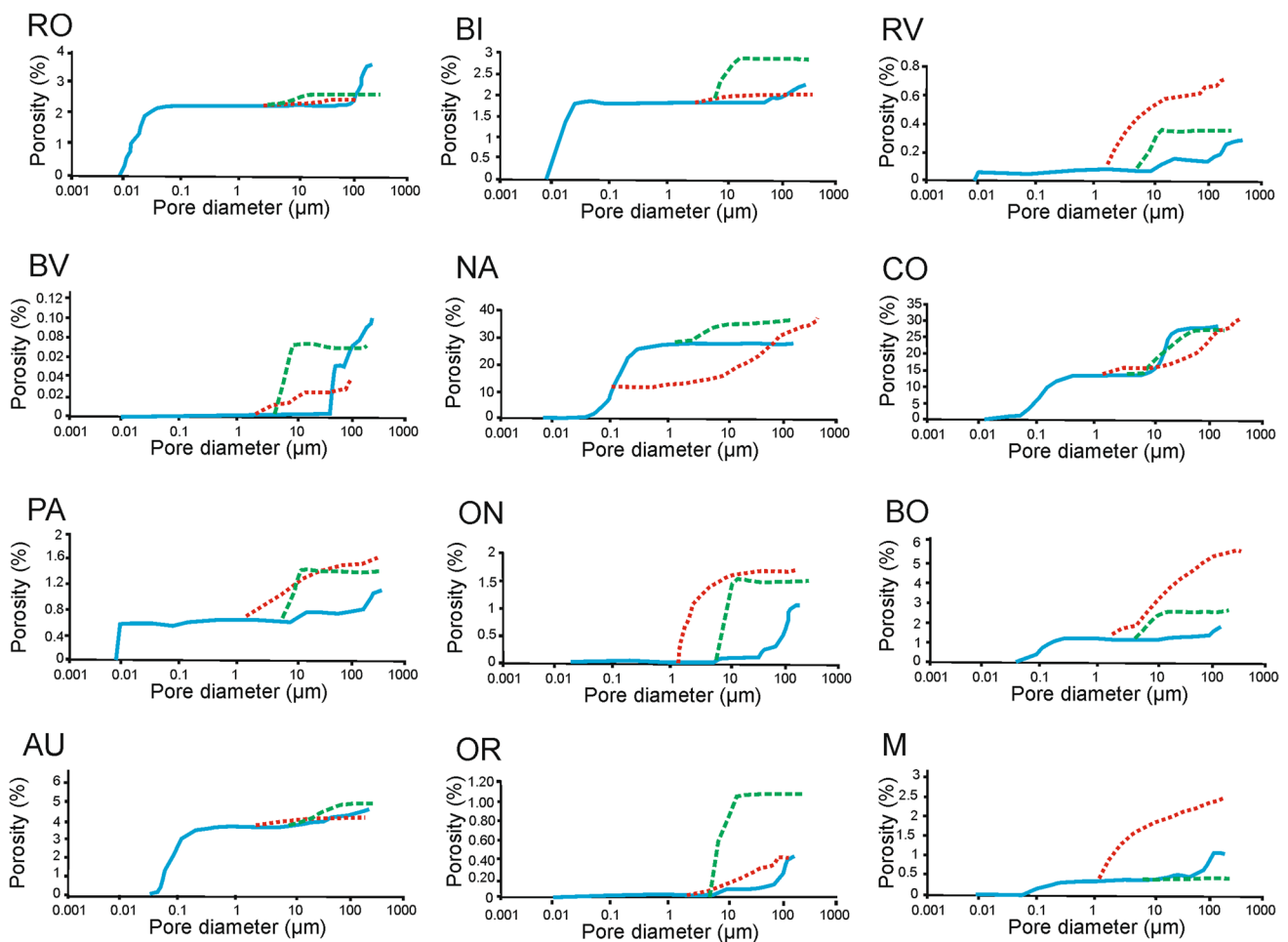


Fig. 4 Cumulative curve (%) of the pore-size distribution obtained by the contribution from the various methods: MIP (blue line), DIA (red dotted line) and m-CT (green dashed line)

Total porosity estimated through the appropriate combination of the different methods generally aligns with MIP data, particularly for rocks characterized by micropores (such as Asiago stones, RO and BI, or Verona stones, BV and RV; see the data in Table 6). However, when macroporosity is present (as seen in Nanto and Costozza stones, NA and CO), the combination of MIP with DIA and m-CT yields a more accurate assessment of the pore system. This is because a significant portion of macro-pores falls beyond the resolution capabilities of MIP. In fact, the cumulative curves generated by MIP often indicate an underestimation of macro-pores, whereas DIA and m-CT results accurately capture them. The standard deviations, calculated through a comparison between the MIP data and the two reconstructed cumulative pore size curves (see Table 6), highlight a strong correlation between total porosity measured by MIP and the combination of MIP data with DIA and m-CT for samples with low porosity dominated by small-sized pores. However, for rocks with a prevalence of large pores, MIP tends to be less reliable. This behaviour is particularly noticeable in the Nanto Stone (sample NA), where we observed standard deviations exceeding 6 (Table 6), whereas for the other samples, we find a good agreement in the data. On the other hand, relying solely on either DIA on SEM-BSE images or m-CT as analytical techniques to determine porosity in rocks with a high percentage of micropores can pose certain challenges. Although it is possible to reduce the lower threshold limit of DIA and m-CT by enhancing resolution (e.g., increasing magnification during image acquisition at the SEM for DIA or reducing the analysed sample volume for m-CT), other issues may arise. These include concerns about sample representativeness or potential increases in analytical time and analytical costs when enlarging the area or volume of the sample to ensure representativeness.

Conclusion

Porosity plays a crucial role in the decay of stones, primarily regulating the penetration and circulation of water, which leads to various physical and chemical deterioration processes affecting stones-built heritage. The comprehensive understanding of a rock's pore system is of paramount importance, as it profoundly impacts the physical and mechanical characteristics of stones used in construction. Mechanical and hydraulic properties are significantly influenced by porosity, and any changes due to deterioration or dissolution can lead to complex effects on the rock's behaviour under external stresses, potentially resulting in failure or altering the geomechanical properties of rock masses. Surprisingly, abundant porosity or large pores, often considered a weakness, can offer advantageous properties such as improved thermal and acoustic insulation, contributing

to enhanced energy efficiency. To accurately predict decay, assess conservation treatments, and develop effective remediation strategies for preserving cultural heritage structures, precise and reliable determination of the pore structure in rocks is an essential aspect that requires careful consideration.

In this study, we analysed the porosity of 12 carbonate rocks commonly found in Italian cultural heritage using mercury intrusion porosimetry (MIP), digital imaging analysis (DIA) of SEM-BSE images, and micro-computed tomography (m-CT). We discussed the results while considering the specific limitations, advantages, and disadvantages of each method. MIP is highly effective at measuring small pores, but it has significant limitations when it comes to measuring larger pores, particularly those with dimensions exceeding 250 μm , which it cannot detect. Although DIA of SEM-BSE images and m-CT are powerful techniques, they may provide insufficient data for samples with an abundance of micropores, as observed in numerous carbonate stones. This limitation arises from the resolution of these techniques, which lead to a lower threshold limit of 0.5 μm for DIA and 4.75 μm for m-CT in our case.

MIP, on the other hand, appears to provide a better description of pore-size distribution, as most samples exhibit a significant fraction of porosity below the lower threshold limits of DIA. However, MIP tends to overestimate the volume of micropores due to the “ink-bottle effect”, resulting in erroneous pore size distribution curves. Both DIA and m-CT provide good quantitative estimations, although they require certain approximations. While MIP, as an indirect method, focusses on open pores, which are critical in deterioration processes, DIA and m-CT consider all types of pores without distinguishing between closed and open porosity. In addition to the resolution issues discussed earlier for DIA and m-CT, it is worth noting that DIA provides data in two dimensions (pores segmentation is performed on microphotographic images), whereas m-CT reproduces the 3D volumetric pore geometry of the samples. However, DIA is the technique that offers the highest representativeness in terms of sample dimensions and is capable of detecting and characterising even large pores, some of which can be as large as centimetres in size. When the majority of pores are concentrated near the detection limit of a specific analytical method, especially in cases of very low porosity, the uncertainty in porosity measurement may be on the same order of magnitude as the measured value. Generally, MIP measurements are reliable for rocks with small pores and low porosity values, unless the fraction of micropores (e.g., below 0.2 μm) is dominant. In such cases, an additional complementary analytical technique, such as nitrogen adsorption, is required. As for DIA, the reliability of measuring small pores and low porosity depends on the image resolution, which defines both the lower dimensional threshold and

the pore size range near it. On the other hand, m-CT has significant limitations when dealing with small pore sizes. Consequently, in this scenario, we may expect that the error could be of the same order of magnitude or even higher than the values obtained for rocks characterized by low porosity and small pore size.

Considering these limitations, we extrapolated the total porosity of the studied samples by comparing data from MIP, DIA and m-CT within two specific “overlapping pore ranges” (OPR-1 and OPR-2). This approach allowed us to determine appropriate threshold limits in the pore size distribution curves obtained from the different methods, enabling their combination (e.g., MIP + DIA and MIP + m-CT) to provide a reliable characterization of the entire pore system.

Given that carbonate rocks, like those analysed in this article, are commonly used materials in cultural heritage, and considering the significance of porosity in various deterioration mechanisms such as salt crystallisation and freeze–thaw cycles, a reliable assessment of the pore structure using the proposed procedure to obtain accurate measurements of total porosity and pore size distribution is essential. This knowledge will greatly support heritage conservation efforts in historical towns and cities.

Acknowledgements The authors would like to express their gratitude to Barchi L. from the Department of Chemistry, Life Sciences and Environmental Sustainability at the University of Parma, Italy, for his invaluable contribution in conducting the MIP analyses. Additionally, the authors would like to thank Tauro L. from the Department of Geosciences at the University of Padova, Italy, for his assistance in preparing the thin sections.

Author contributions SS: writing—original draft, data curation; CC: writing, data curation, review and editing; LM: writing—review and editing; MM: review and editing; FB: review and editing, MIP analysis; CM: conceptualization, writing—review and editing, supervision.

Funding Open access funding provided by Università degli Studi di Padova within the CRUI-CARE Agreement. The authors have not disclosed any funding.

Data availability The data that support the findings of this study are available from the corresponding author, [CC], upon reasonable request.

Declarations

Conflict of interest The authors declare no competing interests.

Open Access This article is licensed under a Creative Commons Attribution 4.0 International License, which permits use, sharing, adaptation, distribution and reproduction in any medium or format, as long as you give appropriate credit to the original author(s) and the source, provide a link to the Creative Commons licence, and indicate if changes were made. The images or other third party material in this article are included in the article's Creative Commons licence, unless indicated otherwise in a credit line to the material. If material is not included in the article's Creative Commons licence and your intended use is not

permitted by statutory regulation or exceeds the permitted use, you will need to obtain permission directly from the copyright holder. To view a copy of this licence, visit <http://creativecommons.org/licenses/by/4.0/>.

References

- Anovitz LM, Cole DR (2015) Characterization and analysis of porosity and pore structure. *Rev Mineral Geochem* 80:61–164. <https://doi.org/10.2138/rmg.2015.80.04>
- Arnold A, Zehnder K (1990) Salt weathering on monuments. In: The conservation of monuments in the Mediterranean Basin: the influence of coastal environment and salt spray on limestone and marble. Proceedings of the 1st international symposium, Bari, 7–10 June 1989. Ed. Grafo, Bari, pp 3–58
- Barbera G, Barone G, Crupi V, Longo F, Maisano G, Majolino D, Mazzoleni P, Raneri S, Teixeira J, Venuti V (2014) A multi-technique approach for the determination of the porous structure of building stone. *Eur J Mineral* 26:189–198. <https://doi.org/10.1127/0935-1221/2014/0026-2355>
- Benavente D (2011) Why pore size is important in the deterioration of porous stones used in the built heritage. *Rev Soc Esp Miner* 15:41–42
- Benavente D, del Cura MG, Fort R, Ordóñez S (2004) Durability estimation of porous building stones from pore structure and strength. *Eng Geol* 74–1:113–127. <https://doi.org/10.1016/j.enggeo.2004.03.005>
- Benavente D, Such-Basañez I, Fernandez-Cortes A, Pla C, Cazorla-Amoros D, Cañaveras JC, Sanchez-Moral S (2021) Comparative analysis of water condensate porosity using mercury intrusion porosimetry and nitrogen and water adsorption techniques in porous building stones. *Constr Build Mater* 288:123131. <https://doi.org/10.1016/j.conbuildmat.2021.123131>
- Brantut N, Baker M, Hansen LN, Baud P (2018) Microstructural control of physical properties during deformation of porous limestone. *J Geophys Res Solid* 123:4751–4764. <https://doi.org/10.1029/2018JB015636>
- Bugini R, Laurenzi Tabasso M, Realini M (2000) Rate of formation of black crusts on marble. A case study. *J Cult Herit* 1:111–116. [https://doi.org/10.1016/S1296-2074\(00\)00161-8](https://doi.org/10.1016/S1296-2074(00)00161-8)
- Cardell C, Benavente D, Rodríguez-Gordillo J (2008) Weathering of limestone building material by mixed sulfate solutions. Characterization of stone microstructure, reaction products and decay forms. *Mat Char* 59:1371–1385. <https://doi.org/10.1016/j.matchar.2007.12.003>
- Chappard D, Legrand E, Haettich B, Chalès G, Auvinet B, Eschard JP, Hamelin JP, Baslé MF, Audran M (2001) Fractal dimension of trabecular bone: comparison of three histomorphometric computed techniques for measuring the architectural two-dimensional complexity. *J Pathol* 195:515–521. <https://doi.org/10.1002/path.970>
- Charola AE (2000) Salts in the deterioration of porous materials: an overview. *J Am Inst Conserv* 39–3:327–343. <https://doi.org/10.1179/019713600806113176>
- Choquette PW, Pray LC (1970) Geologic nomenclature and classification of porosity in sedimentary carbonates. *AAPG Bull* 54–2:207–250. <https://doi.org/10.1306/5D25C98B-16C1-11D7-8645000102C1865D>
- Cnudde V, Cwirzen A, Masschaele B, Jacobs PJS (2009) Porosity and microstructure characterization of building stones and concretes. *Eng Geol* 103:76–83. <https://doi.org/10.1016/j.enggeo.2008.06.014>

- Coletti C, Cultrone G, Maritan L, Mazzoli C (2016) Combined multi-analytical approach for study of pore system in bricks: How much porosity is there? *Mater Charact* 121:82–92. <https://doi.org/10.1016/j.matchar.2016.09.024>
- Dubinini MM (1979) Characterization of porous solids. In: Society of chemical industry. London, p 1
- Dal Ferro N, Delmas P, Duwig C, Simonetti G, Morari F (2012) Coupling X-ray microtomography and mercury intrusion porosimetry to quantify aggregate structures of a cambisol under different fertilisation treatments. *Soil Tillage Res* 119:13–21. <https://doi.org/10.1016/j.still.2011.12.001>
- Dal Sasso G, Maritan L, Salvatori S, Mazzoli C, Artioli G (2014) Discriminating pottery production by image analysis: a case study of Mesolithic and Neolithic pottery from Al Khiday (Khartoum, Sudan). *J Archaeol Sci* 46:125–143. <https://doi.org/10.1016/j.jas.2014.03.004>
- De Boever W, Derluyn HD, Van Hoorebeke L, Cnudde V (2015) Data-fusion of high resolution X-ray CT, SEM and EDS for 3D and pseudo-3D chemical and structural characterization of sandstone. *Micron* 74:15–21. <https://doi.org/10.1016/j.micron.2015.04.003>
- De Kock T, Turmel A, Fronteau G, Cnudde V (2017) Rock fabric heterogeneity and its influence on the petrophysical properties of a building limestone: Lede stone (Belgium) as an example. *Eng Geol* 216:31–41. <https://doi.org/10.1016/j.enggeo.2016.11.007>
- De Quervain F (1967) Technische Gesteinskunde. Lehrbücher und Monographien aus dem Gebiete der exakten Wissenschaften. Mineralogisch-geotechnische Reihe, 1
- Di Benedetto C, Cappelletti P, Favaro M, Graziano SF, Langella A, Calcaterra D, Colella A (2015) Porosity as key factor in the durability of two historical building stones: Neapolitan Yellow Tuff and Vicenza Stone. *Eng Geol* 193:310–319. <https://doi.org/10.1016/j.enggeo.2015.05.006>
- Doehne E (2002) Salt weathering: a selective review. *Geol Soc Lond Spec Publ* 205–1:51–64. <https://doi.org/10.1144/GSL.SP.2002.205.01.05>
- Fitzner B, Basten D (1994) Gesteinsporosität—Klassifizierung, meßtechnische Erfassung und Bewertung ihrer Verwitterungsrelevanz—Jahresberichte aus dem Forschungsprogramm “Steinzenerfall-Steinkonservierung” 1992, Förderprojekt des Bundesministers für Forschung und Technologie. Ed. Verlag Ernst & Sohn, Berlin
- Fusi N, Martínez-Martínez J (2013) General characterization of the mechanical behaviour of different volcanic rocks with respect to alteration. *Eng Geol* 166:272–282. <https://doi.org/10.1016/j.enggeo.2013.10.002>
- Gabriele F, Ranaldi R, Bruno L, Casieri C, Rugnini L, Spreti N (2023) Biodeterioration of stone monuments: studies on the influence of bioreceptivity on cyanobacterial biofilm growth and on the biocidal efficacy of essential oils in natural hydrogel. *Sci Total Environ* 870:161901. <https://doi.org/10.1016/j.scitotenv.2023.161901>
- Galaup S, Liu Y, Cerepi A (2012) New integrated 2D–3D physical method to evaluate the porosity and microstructure of carbonate and dolomite porous system. *Microporous Mesoporous Mater* 154:175–186. <https://doi.org/10.1016/j.micromeso.2011.12.021>
- García-del-Cura MA, Benavente D, Martínez-Martínez J, Cueto N (2012) Sedimentary structures and physical properties of travertine and carbonate tufa building stone. *Constr Build Mat* 28:456–467. <https://doi.org/10.1016/j.conbuildmat.2011.08.042>
- Giesche H (2006) Mercury porosimetry: a general (practical) overview. *Part Part Syst Charact* 23:9–19. <https://doi.org/10.1002/ppsc.200601009>
- Gregg SJ, Sing KSW (1983) Adsorption, surface area, and porosity. *Berichte der Bunsengesellschaft für Physikalische Chemie* 86–10:957. <https://doi.org/10.1002/bbpc.19670710837>
- Grossi CM, Brimblecombe P, Harris I (2007) Predicting long term freeze-thaw risks on Europe built heritage and archaeological sites in a changing climate. *Sci Total Environ* 377:273–281. <https://doi.org/10.1016/j.scitotenv.2007.02.014>
- Grove C, Jerram DA (2011) jPOR: an ImageJ macro to quantify total optical porosity from blue-stained thin sections. *Comput Geosci* 37(11):1850–1859. <https://doi.org/10.1016/j.cageo.2011.03.002>
- Klopfer H (1985) Feuchte. In: Lutz P, Jenisch R, Klopfer H et al (eds) *Lehrbuch der Bauphysik*. Ed. Teubner, Stuttgart
- Kodikara J, Barbour SL, Fredlund DG (1999) Changes in clay structure and behavior due to wetting and drying. In: 8th Australian-New Zealand conference on geomechanics, Australian Geomechanics, Hobart
- Koubaa Y, Jamei M, Guiras H (2018) Hydro-mechanical properties of highly porous limestone rock used for historic monuments in North-East Tunisia. *J Civ Environ Eng* 8(3):310. <https://doi.org/10.4172/2165-784X.1000310>
- León y León CA (1998) New perspectives in mercury porosimetry. *Adv Colloid Interface Sci* 76:341–372. [https://doi.org/10.1016/S0001-8686\(98\)00052-9](https://doi.org/10.1016/S0001-8686(98)00052-9)
- Maritan L, Piovesan R, Dal Sasso G, Baklouti S, Casas L, Mazzoli C, Salmasso L, Corain L (2020) Comparison between different image acquisition methods for grain-size analysis and quantification of ceramic inclusions by digital image processing: how much similar are the results? *Archaeol Anthropol Sci* 12:167. <https://doi.org/10.1007/s12520-020-01096-0>
- Mineo S, Pappalardo G (2022) Non-destructive rock porosity estimation by InfraRed Thermography applied to natural stones. *Constr Build Mat* 342-B:127950. <https://doi.org/10.1016/j.conbuildmat.2022.127950>. ISSN:0950-0618
- Molina E, Benavente D, Sebastian E, Cultrone G (2015) The influence of rock fabric in the durability of two sandstones used in the Andalusian Architectural Heritage (Montoro and Ronda, Spain). *Eng Geol* 197:67–81. <https://doi.org/10.1016/j.enggeo.2015.08.009>
- Moro F, Böhni H (2002) Ink-bottle effect in mercury intrusion porosimetry of cement-based materials. *J Colloid Interface Sci* 246:135–149. <https://doi.org/10.1006/jcis.2001.7962>
- Ng K, Santamarina JC (2023) Mechanical and hydraulic properties of carbonate rock: the critical role of porosity. *J Rock Mech Geotech Eng* 15:814–825. <https://doi.org/10.1016/j.jrmge.2022.07.017>
- Niazi FS, Piñán-Llamas A, Fekadu F (2021) Impact of chemical weathering on microstructures and mechanical properties of karstic limestone. *Geotech Lett* 11(4):281–293. <https://doi.org/10.1680/jgele.21.00055>
- Nicholson DT (2001) Pore properties as indicators of breakdown mechanism in experimentally weathered limestones. *Earth Surf Process Landf* 26:819–838. <https://doi.org/10.1002/esp.228>
- Noiriel C (2015) Resolving time-dependent evolution of pore-scale structure, permeability and reactivity using X-ray microtomography. *Rev Mineral Geochem* 80:247–285. <https://doi.org/10.2138/rmg.2015.80.08>
- Pappalardo G, Punturo R, Mineo S, Contrafatto L (2017) The role of porosity on the engineering geological properties of 1669 lavas from Mount Etna. *Eng Geol* 221:16–28. <https://doi.org/10.1016/j.enggeo.2017.02.020>
- Rasband WS (1997–2015) ImageJ, U.S. National Institutes of Health, Bethesda, Maryland, USA. <http://imagej.nih.gov/ij/>
- Rigby SP, Fletcher RS, Riley SN (2004) Characterization of porous solids using integrated nitrogen sorption and mercury porosimetry. *Chem Eng Sci* 59:41–51. <https://doi.org/10.1016/j.ces.2003.09.017>
- Rijniers LA, Pel L, Huinink HP, Kopinga K (2005) Salt crystallization as damage mechanism in porous building materials—a nuclear magnetic resonance study. *Magn Reson Imaging* 23:273–276. <https://doi.org/10.1016/j.mri.2004.11.023>
- Rodríguez-Navarro C, Doehne E (1999) Salt weathering: Influence of evaporation rate, supersaturation and crystallization pattern. *Earth*

- Surf Process Landf 24:191–209. [https://doi.org/10.1002/\(SICI\)1096-9837\(199903\)24:3%3C191::AID-ESP942%3E3.0.CO;2-G](https://doi.org/10.1002/(SICI)1096-9837(199903)24:3%3C191::AID-ESP942%3E3.0.CO;2-G)
- Ruedrich J, Siegesmund S (2007) Salt and ice crystallization in porous sandstones. *Environ Geol* 52–2:225–249. <https://doi.org/10.1007/s00254-006-0585-6>
- Ruedrich J, Kirchner D, Siegesmund S (2011) Physical weathering of building stones induced by freeze–thaw action: a laboratory long-term study. *Environ Earth Sci* 63:1573–1586. <https://doi.org/10.1007/s12665-010-0826-6>
- Salvini S, Bertonecello R, Coletti C, Germinario L, Maritan L, Massironi M, Pozzobon R, Mazzoli C (2022) Recession rate of carbonate rocks used in cultural heritage: textural control assessed by accelerated ageing tests. *J Cult Herit* 57–6:154–164. <https://doi.org/10.1016/j.culher.2022.08.010>
- Salvini S, Coletti C, Maritan L, Massironi M, Spiess R, Mazzoli C (2023) Petrographic characterization and durability of carbonate stones used in UNESCO World Heritage sites in northeastern Italy. *Environ Earth Sci*. <https://doi.org/10.1007/s12665-022-10732-y>
- Sawdy A, Price C (2005) Salt damage at Cleeve Abbey, England. Part II: seasonal variability of salt distribution and implications for sampling strategies. *J Cult Herit* 6–3:269–275. <https://doi.org/10.1016/j.culher.2005.02.004>
- Scherer GW (1999) Crystallization in pores. *Cem Concr Res* 29:1347–1358. [https://doi.org/10.1016/S0008-8846\(99\)00002-2](https://doi.org/10.1016/S0008-8846(99)00002-2)
- Scrivano S, Gaggero L, Aguilar JG (2018) Micro-porosity and mineralogical features influences on decay: experimental data from four dimension stones. *Constr Build Mater* 173:342–349. <https://doi.org/10.1016/j.conbuildmat.2018.04.041>
- Siegesmund S, Dürrast H (2011) Physical and mechanical properties of rocks. In: Siegesmund S, Snethlage R (eds) *Stone in architecture*. Springer, Berlin, Heidelberg, pp 97–225
- Steiger M (2005) Crystal growth in porous materials—I: the crystallisation pressure of large crystals. *J Cryst Growth* 282:455–469. <https://doi.org/10.1016/j.jcrysgro.2005.05.007>
- Steiger M, Charola AE (2011) Weathering and deterioration. In: Siegesmund S, Snethlage R (eds) *Stone in architecture. Properties, durability*, 4th edn. Springer, Berlin, pp 227–316
- Warscheid T, Braams J (2000) Biodeterioration of stone: a review. *Int Biodeterior Biodegrad* 46–4:343–368. [https://doi.org/10.1016/S0964-8305\(00\)00109-8](https://doi.org/10.1016/S0964-8305(00)00109-8)
- Yang H, Xu Z, Jiang M (2023) Theoretical model for the effect of porosity on correlations of point load tests of rocks. *Géotech Lett* 13(3):1–7. <https://doi.org/10.1680/jgele.23.00022>
- Zong Y, Yu X, Zhu M, Lu S (2015) Characterizing soil pore structure using nitrogen adsorption, mercury intrusion porosimetry, and synchrotron-radiation-based X-ray computed microtomography techniques. *J Soils Sedim* 15:302–312. <https://doi.org/10.1007/s11368-014-0995-0>

Publisher's Note Springer Nature remains neutral with regard to jurisdictional claims in published maps and institutional affiliations.